

# Interplay of superconductivity and Ce 4*f* magnetism in CeFeAs<sub>1-x</sub>P<sub>x</sub>O<sub>0.95</sub>F<sub>0.05</sub>

Yongkang Luo,<sup>1</sup> Han Han,<sup>1</sup> Shuai Jiang,<sup>1</sup> Xiao Lin,<sup>1</sup> Yuke Li,<sup>1</sup> Jianhui Dai,<sup>1</sup> Guanghan Cao,<sup>1,2</sup> and Zhu-an Xu<sup>1,2,\*</sup>

<sup>1</sup>Department of Physics, Zhejiang University, Hangzhou 310027, China

<sup>2</sup>State Key Laboratory of Silicon Materials, Zhejiang University, Hangzhou 310027, China

(Received 25 August 2010; revised manuscript received 29 November 2010; published 4 February 2011)

We performed a systematic investigation of the physical properties of CeFeAs<sub>1-x</sub>P<sub>x</sub>O<sub>0.95</sub>F<sub>0.05</sub> ( $0 \leq x \leq 1$ ) by measuring electrical resistivity, magnetization, and specific heat. Superconductivity (SC) was observed in a wide range of P doping,  $0 \leq x < 0.55$ , with a maximum  $T_c \approx 21.3$  K at  $x = 0.15$ . Both the  $x = 0$  and 0.53 samples show a reentrance behavior near the antiferromagnetic and ferromagnetic ordering temperatures of the Ce 4*f* spins, respectively. An antiferromagnetic-to-ferromagnetic (FM) evolution of Ce 4*f* electrons was observed around  $x = 0.45$  and SC competes with the ferromagnetic order of Ce 4*f* electrons in this region. Our results provide clear evidence for the SC-FM competition caused by the interlayer coupling in the cerium-containing iron pnictides.

DOI: [10.1103/PhysRevB.83.054501](https://doi.org/10.1103/PhysRevB.83.054501)

PACS number(s): 74.70.Dd, 75.30.Mb, 74.62.Dh, 74.62.Bf

## I. INTRODUCTION

The discovery of 26 K superconductivity (SC) in LaFeAsO<sub>1-y</sub>F<sub>y</sub> (Ref. 1) has triggered enormous interest in the iron pnictides;<sup>2-5</sup>  $T_c$  can be raised up to about 56 K when La is replaced by other rare earth elements.<sup>6,7</sup> The parent compounds of these so-called 1111-type pnictides, RFePO ( $R$  = rare earths;  $P$  = P, As), are of the ZrCuSiAs-type crystal structure with a unique FeP layer sandwiched by the RO layers.<sup>8</sup> The former acts as a conducting layer and the latter as insulating building blocks. Usually, RFeAsO is a bad metal with a structure distortion and an antiferromagnetic (AFM) instability around 130 ~ 150 K.<sup>9</sup> Superconductivity can be obtained by chemical doping or uniaxial pressure when the AFM long-range order is suppressed.

Among all these RFePO's, the member  $R = \text{Ce}$  is an appealing candidate to investigate the interaction between the 3*d* and 4*f* electrons. CeFeAsO is an itinerant AFM bad metal with Ce 4*f* moments showing AFM order below 4 K.<sup>3,10</sup> SC can be obtained by F doping on the O site, which introduces extra electrons into the conducting FeAs layer.<sup>3</sup> The phase diagram of CeFeAsO<sub>1-y</sub>F<sub>y</sub> has been mapped by a study of neutron scattering;<sup>10</sup> SC appears around  $y = 0.06$  and the Fe<sup>2+</sup>-related AFM instability is completely suppressed simultaneously, while the structure distortion can persist to a higher F<sup>-</sup> doping level. Meanwhile, CeFePO is a paramagnetic (PM) heavy-fermion (HF) metal with ferromagnetic (FM) fluctuations.<sup>11,12</sup> The isovalent P-As substitution within the FeAs layer is an accessible approach to tune the interplay between Fe 3*d* and Ce 4*f* correlations, and to reveal the possible magnetic quantum critical points (QCP's) of either *d* or *f* electrons.<sup>13,14</sup> Moreover, superconductivity can be induced due to the chemical pressure caused by P-As substitution in both 1111- and 122-type iron pnictides.<sup>15-18</sup> The phase diagram of CeFeAs<sub>1-x</sub>P<sub>x</sub>O has been reported in previous experimental studies,<sup>12,19</sup> where the two QCP's, corresponding to the disappearance of Fe<sup>2+</sup> and Ce<sup>3+</sup> long-range magnetic order, appear at  $x = 0.4$  and 0.92, respectively. However, no superconductivity was observed in the whole P doping range of  $0 \leq x \leq 1$  in CeFeAs<sub>1-x</sub>P<sub>x</sub>O. On the other hand, a turning point of Ce *f*-electron ordering from AFM to FM was found at  $x = 0.37$ . The strong FM correlation of Ce 4*f* electrons

should account for the absence of SC. Furthermore, HF-like behavior was found for  $x > 0.92$ . These observations provide clear evidence for the Ce *f*-electron Kondo effect driven by the interlayer *d-f* coupling. It is very interesting to see if this *d-f* coupling can also play a role when the Fe 3*d* electrons exhibit SC, as in the F-doped CeFeAsO compound.

In this paper, we report a systematic investigation of physical properties of CeFeAs<sub>1-x</sub>P<sub>x</sub>O<sub>0.95</sub>F<sub>0.05</sub> ( $0 \leq x \leq 1$ ) by electrical resistivity, magnetization, and specific heat measurements. For  $x = 0$ , CeFeAsO<sub>0.95</sub>F<sub>0.05</sub> with  $T_c = 13.3$  K is on the boundary of the SC region in the phase diagram. When it is doped with P, SC develops in the region  $0 \leq x < 0.55$  with the maximum  $T_c \approx 21.3$  K at  $x = 0.15$ . An AFM-to-FM evolution of Ce 4*f* spins was observed around  $x = 0.45$ , and no HF behavior appears in the entire P doping region. Compared with other doped 1111-type pnictide series,<sup>10,20,21</sup> the CeFeAs<sub>1-x</sub>P<sub>x</sub>O<sub>0.95</sub>F<sub>0.05</sub> system demonstrates a peculiar region where there is a coexistence of SC and Ce 4*f* magnetism, both AFM and FM, and our work reveals the interplay between the *d*-electron superconducting pairing and the *f*-electron magnetism.

This paper is organized as follows: In Sec. II, we briefly describe the experimental details. In Sec. III, the results and discussions are presented; the structural information, the Fe 3*d* SC, the Ce 4*f* magnetism, and the phase diagram are given in Secs. III A, III B, III C, and III D, respectively. Section IV contains the summary and conclusion. For supplementary information, the experimental results for CeFePO<sub>1-y</sub>F<sub>y</sub> are presented in the Appendix.

## II. EXPERIMENT

We have synthesized a series of CeFeAs<sub>1-x</sub>P<sub>x</sub>O<sub>0.95</sub>F<sub>0.05</sub> ( $0 \leq x \leq 1$ , 16 samples in total) polycrystalline samples by the solid state reaction method. Ce, Fe, As, P, CeF<sub>3</sub>, and CeO<sub>2</sub> of high purity ( $\geq 99.95\%$ ) were used as starting materials. First, CeAs (or CeP) was presynthesized by reacting Ce disks and As (or P) powders at  $\sim 1300$  K for 72 h. FeAs (or FeP) was presynthesized by reacting Fe and As (or P) powders at around 970 K for 20 h. Second, powders of CeAs, CeP, CeO<sub>2</sub>, CeF<sub>3</sub>, FeAs, and FeP were weighed according to the stoichiometric ratio,

thoroughly ground, and pressed into a pellet under a pressure of 600 MPa in an argon-filled glove box. The pellet was sealed into an evacuated quartz tube, which was then slowly heated to 1430–1470 K and kept at that temperature for 50 h.

Powder x-ray diffraction (XRD) was performed at room temperature using a D/Max-rA diffractometer with Cu  $K\alpha$  radiation and a graphite monochromator. Lattice parameters were refined by a least-squares fit using at least 20 XRD peaks. Electrical resistivity and specific heat were measured on a Quantum Design physical property measurement system (PPMS-9). The dc magnetization measurement was carried out on a Quantum Design magnetic property measurement system (MPMS-5) employing both zero-field-cooling (ZFC) and field-cooling (FC) protocols.

### III. RESULTS AND DISCUSSION

#### A. Structural information

Figure 1 shows the XRD patterns of six representative samples of  $\text{CeFeAs}_{1-x}\text{P}_x\text{O}_{0.95}\text{F}_{0.05}$ . Other samples show similar XRD patterns (not shown here). No obvious impurity phases can be detected, and all the peaks can be well indexed based on the  $P4/nmm$  (No. 129) space group with tetragonal  $\text{ZrCuSiAs}$ -type structure, suggesting the high purity of these samples. All the peaks shift to the right with increasing P content, indicating the shrinkage of both  $a$  and  $c$  lattice constants. It is also found that the  $c$  axis decreases faster than the  $a$  axis, as shown in the inset of Fig. 1, similar to the case of  $\text{CeFeAs}_{1-x}\text{P}_x\text{O}$ .<sup>12</sup> It is interesting that F doping in the two end compounds  $\text{CeFeAsO}$  and  $\text{CeFeAsP}$  causes different changes in the lattice parameters. In  $\text{CeFeAsO}$ , there is a decrease in both the  $a$  and  $c$  axes due to F doping, while in  $\text{CeFePO}$ , on the contrary, there is an increase in the  $c$  axis due to F doping. Such an effect of F doping on the lattice constants was also observed in  $\text{LaFePO}_{1-y}\text{F}_y$ .<sup>22</sup>

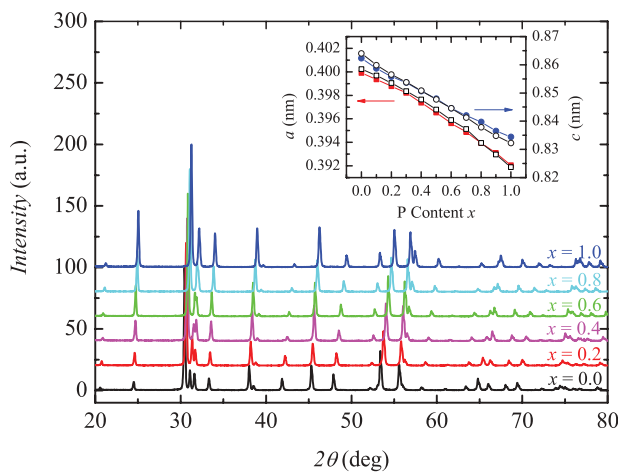


FIG. 1. (Color online) Room-temperature XRD patterns of representative  $\text{CeFeAs}_{1-x}\text{P}_x\text{O}_{0.95}\text{F}_{0.05}$  compounds ( $x = 0, 0.2, 0.4, 0.6, 0.8$ , and  $1.0$ ). Inset: variations of lattice constants  $a$  (squares) and  $c$  (circles) with P doping content  $x$  in steps of  $\Delta x = 0.1$ . The solid symbols stand for  $\text{CeFeAs}_{1-x}\text{P}_x\text{O}_{0.95}\text{F}_{0.05}$ , while the open ones are for  $\text{CeFeAs}_{1-x}\text{P}_x\text{O}$  [taken from our previous report (Ref. 12)].

#### B. Superconductivity

The temperature dependence of resistivity is shown in Figs. 2(a) and 2(b) for all the  $\text{CeFeAs}_{1-x}\text{P}_x\text{O}_{0.95}\text{F}_{0.05}$  ( $0 \leq x \leq 1$ ) samples. Three prominent features can be identified in the profiles of resistivity. (i) The resistivity decreases almost linearly with decreasing temperature for all the samples for temperature above 100 K, confirming the metallicity of F-doped  $\text{CeFeAs}_{1-x}\text{P}_x\text{O}$ . (ii) In the underdoped regime ( $x < 0.15$ ), there is a clear upturn in the  $\rho(T)$  curve at low temperatures. Upon P doping, the upturn is suppressed to lower temperatures, and vanishes in the overdoped regime ( $x > 0.15$ ). This doping-dependent upturn might be associated with the residual structure distortion and/or AFM transition of Fe  $d$  electrons. Actually, according to the phase diagram mapped by neutron scattering on  $\text{CeFeAsO}_{1-y}\text{F}_y$ ,<sup>10</sup> the AFM instability of the  $d$  electrons persists until 6% F doping, and the structure distortion persists to even higher  $\text{F}^-$  concentrations. Thus it is reasonable to claim that these phase transitions could exist in the  $\text{CeFeAs}_{1-x}\text{P}_x\text{O}_{0.95}\text{F}_{0.05}$  system. (iii) No SC is observed down to the lowest measured temperature 2 K for  $x \geq 0.55$  and there is a broad hump around 70 K. Such a hump is reminiscent of the Ruderman-Kittel-Kasuya-Yosida (RKKY) scattering effect.

Now we focus on the resistivity profiles for  $0 \leq x \leq 0.53$ , i.e., the SC regime, presented in Figs. 2(c)–2(f). For  $x = 0$ ,  $\text{CeFeAsO}_{0.95}\text{F}_{0.05}$  is on the verge of the SC regime. As the temperature is lowered down from room temperature, the resistivity decreases almost linearly until 100 K, where an upturn occurs. As the temperature is further reduced, there is a sharp decrease around 13.3 K, followed by a distinct peak at 2.8 K. The latter is reminiscent of the Ce  $4f$  AFM transition in the parent compound  $\text{CeFeAsO}$ ;<sup>23</sup> this is further confirmed by the temperature dependence of the susceptibility [Fig. 3(a)]. The drop around 13.3 K is a superconducting transition as confirmed by the magnetic measurement shown in Fig. 3(a). When the magnetic field increases [see Fig. 2(c)], the resistivity drop becomes less pronounced, the SC transition becomes broader, and the onset transition temperature  $T_c^{\text{on}}$  (defined as the temperature at which the resistivity drops to 90% of the normal state) is suppressed to a lower temperature. As the compound is doped with P, the SC transition becomes much more obvious, and  $T_c^{\text{on}}$  increases to 17.4 K for  $x = 0.05$ , but still no zero resistance is reached. This is due to the reentrance caused by  $\text{Ce}^{3+}$  AFM ordering. When the P content is further increased, i.e.,  $x \geq 0.1$ , zero resistance can be observed, and  $T_c^{\text{on}}$  reaches its maximum 21.3 K for  $x = 0.15$ .  $T_c^{\text{on}}$  begins to go down for  $x > 0.15$ . To see the SC transition clearly, an enlarged plot of the resistivity for  $\text{CeFeAs}_{1-x}\text{P}_x\text{O}_{0.95}\text{F}_{0.05}$  ( $0 \leq x \leq 0.53$ ) is also shown in Figs. 2(e) and 2(f). The SC persists up to  $x = 0.53$ , and again there is an emergent reentrance around 5 K [Fig. 2(d)]. The magnetoresistance measurements confirm a SC transition with  $T_c^{\text{on}} = 7.5$  K. However, when the applied magnetic field is strong enough ( $\mu_0 H > 1$  T), SC is completely suppressed, and the magnetoresistance becomes negative, indicating a FM state of Ce  $4f$  correlation. This FM feature will be discussed in Sec. III C. To our knowledge, this is the first demonstration of coexistence of both AFM and FM order of  $4f$  magnetism with SC in 1111-type pnictides. It should be emphasized that

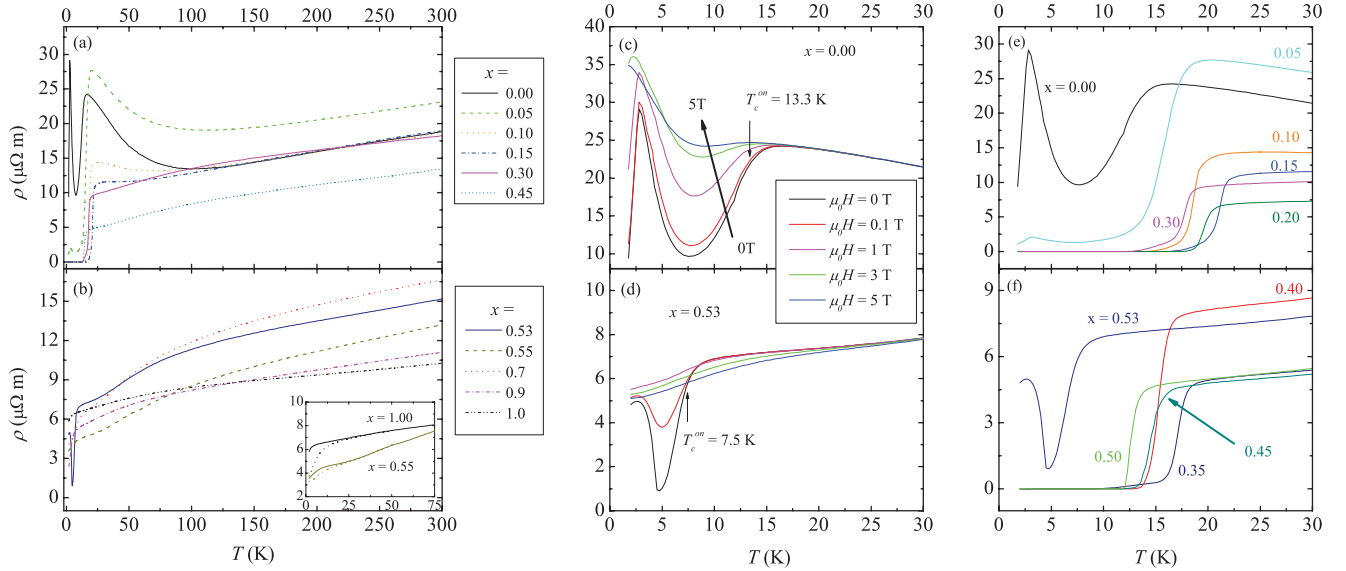


FIG. 2. (Color online) Temperature-dependent resistivity of  $\text{CeFeAs}_{1-x}\text{P}_x\text{O}_{0.95}\text{F}_{0.05}$ . (a),(b) Temperature dependence of selected synthesized samples, for  $x \leq 0.45$  and  $x > 0.45$ , respectively. Inset of (b): resistivity measured under  $\mu_0 H = 0$  (solid) and 5 T (dashed). (c),(d) Reentrance of superconductivity in  $\text{CeFeAsO}_{0.95}\text{F}_{0.05}$  and  $\text{CeFeAs}_{0.47}\text{P}_{0.53}\text{O}_{0.95}\text{F}_{0.05}$  under different fields. (e),(f) Enlarged plot of resistivity in superconducting regime,  $0 \leq x \leq 0.30$  and  $0.35 \leq x \leq 0.53$ , respectively.

all these results are reproducible on different samples with the same composition.

SC of the  $\text{CeFeAs}_{1-x}\text{P}_x\text{O}_{0.95}\text{F}_{0.05}$  ( $0 \leq x \leq 0.53$ ) samples is also confirmed by the temperature-dependent dc magnetic susceptibility measured under  $H = 10$  Oe, as shown in Fig. 3. For  $x = 0$ , no bulk Meissner diamagnetic effect, but only a kink, can be found near the transition temperature on the

$\chi$ - $T$  curve. Upon P doping, the Meissner diamagnetic effect becomes more obvious, and the volume fraction of magnetic shielding reaches more than 70% for the optimal P doping case,  $x = 0.15$ . For  $x = 0.53$ , which is at the right verge of the SC regime, no drop in susceptibility due to the SC transition is observed, and instead a divergency between the ZFC and FC measurements can be found, caused by the Ce 4f FM order (see below). For  $x > 0.53$ , no SC can be identified in either resistivity or susceptibility down to 2 K. For the optimally doped sample ( $x = 0.15$ ), we further measured magnetic susceptibility under different magnetic fields, to manifest the homogeneity of coexisting SC and Ce 4f magnetism [see Fig. 4(a) and Sec. III C for more details].

### C. Ce 4f magnetism

Figure 4 shows the dc magnetic susceptibility measured under 1000 Oe for the representative samples. In the high-temperature range,  $\chi(T)$  increases with decreasing temperature down to  $\sim 150$  K, following a Curie-Weiss law for the whole doping range  $0 \leq x \leq 1$ . The effective moment  $\mu_{\text{eff}}$  is  $2.48\mu_B$  for  $x = 0$ , and  $2.58\mu_B$  for  $x = 1$  [see the inset of Fig. 4(b)], very close to that of a free  $\text{Ce}^{3+}$  ion,  $2.54\mu_B$ . Actually, in the whole P doping range,  $\mu_{\text{eff}}$  does not change much (inset of Fig. 7), and only a slightly increasing trend can be seen. Around  $T$  of 150 K, we observed a change in the slope of the  $1/\chi$ - $T$  curves. This change can be ascribed to the crystal electric field (CEF) effect.<sup>11</sup> As the temperature was lowered, a clear peak was observed at 2.8 K for  $x = 0$ , related to the formation of the  $\text{Ce}^{3+}$  AFM order. When the sample is doped with P,  $\chi(T)$  increases and the peak becomes rounded (or shoulderlike). However, the corresponding AFM ordering temperature ( $T_N$ ) does not change much. When  $x \geq 0.45$  the AFM peak disappears. Moreover, an obvious divergence between ZFC and FC data is seen at lower temperatures for

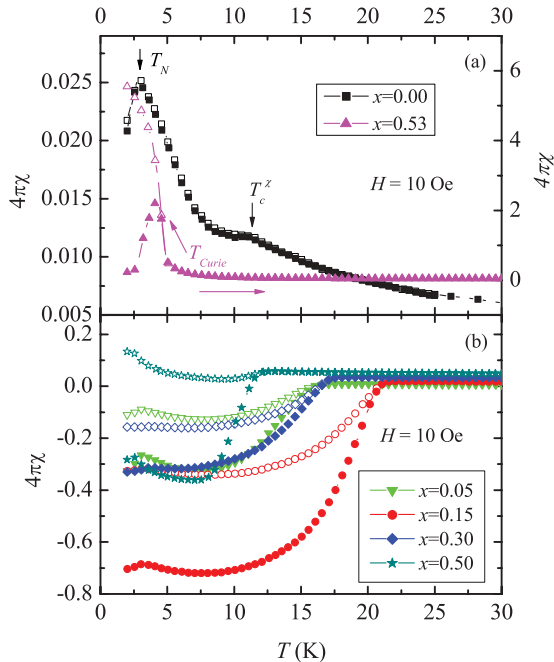


FIG. 3. (Color online) Temperature-dependent dc magnetic susceptibility of  $\text{CeFeAs}_{1-x}\text{P}_x\text{O}_{0.95}\text{F}_{0.05}$ ,  $x \leq 0.53$ , measured under a magnetic field  $H = 10$  Oe. Solid symbols stand for ZFC and open ones for FC data.

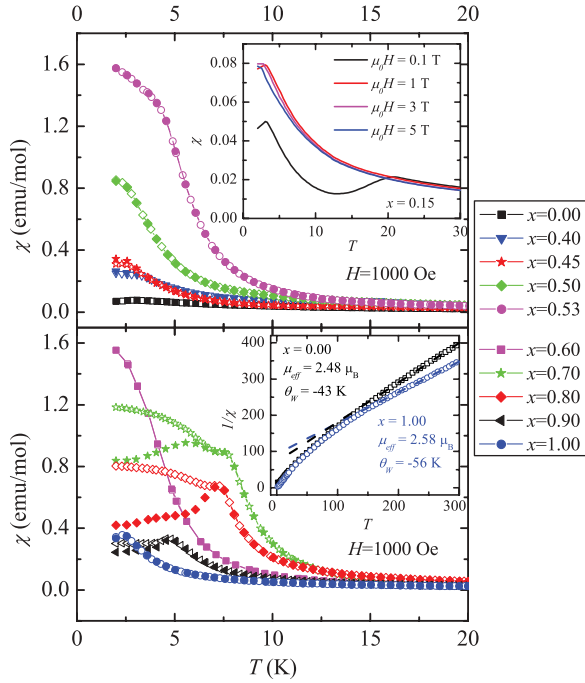


FIG. 4. (Color online) Temperature dependence of dc magnetic susceptibility of  $\text{CeFeAs}_{1-x}\text{P}_x\text{O}_{0.95}\text{F}_{0.05}$  measured under a magnetic field  $H = 1000$  Oe. The solid symbols stand for data measured in ZFC mode, and the open ones in FC mode. Inset of (a): susceptibility of  $x = 0.15$  under various magnetic fields. Inset of (b): Inverse susceptibility of  $x = 0.00$  and  $1.00$  to show the Curie-Weiss behavior above 150 K.

$x > 0.6$ , manifesting the long-range FM-ordered ground state of the Ce  $4f$  electrons.

The inset of Fig. 4(a) shows the magnetic susceptibility measured under  $\mu_0 H = 0.1, 1, 3$ , and  $5$  T for the optimally doped sample ( $x = 0.15$ ) to manifest the homogeneity of the

coexisting SC and Ce  $4f$  magnetism. A small peak is observed around 3 K under 0.1 T. With increasing external field, the peak becomes rounder and shoulderlike; meanwhile its location shifts to a lower temperature. This feature is consistent with the AFM ordering of the  $\text{Ce}^{3+}$  local moments.

Figure 5 shows the magnetic field dependence of magnetization at the fixed temperatures 2 K (solid lines) and 10 K (dashed lines). For  $x = 0$  and  $T = 2$  K, a linear field dependence of magnetization is observed at low fields, and a kink is clearly seen, indicating a possible spin flop in the AFM state of  $\text{Ce}^{3+}$ . When  $x$  increases, SC is enhanced. The flux pinning effect is more evident and a hysteresis loop is observed; see Fig. 5(b). Due to the contribution from the  $\text{Ce}^{3+}$  moments, the Bean-like hysteresis loop is tilted. The AFM-correlated Ce  $4f$  ground state persists to  $x \sim 0.45$ , where  $M(H)$  starts to increase rapidly for small fields and tends to saturate at higher fields. For  $0.6 \leq x \leq 0.9$ , a clear FM hysteresis loop can be observed and the saturated  $M$  value reaches a maximum around  $x = 0.7$  [see Fig. 5(f)]. The largest saturated magnetic moment is about  $0.92\mu_B$ , close to the  $1\mu_B$  expected for a  $\text{Ce}^{3+}$  doublet ground state (Refs. 11 and 24). For  $x = 1$ , the hysteresis loop is hardly observable down to 2 K, while the saturation tendency persists.

Therefore, both the temperature-dependent susceptibility and isothermal magnetization exhibit a typical FM long-range order of the  $\text{Ce}^{3+}$  moments when  $x > 0.6$ . This is consistent with previous resistivity profiles. In Fig. 2(b), a rapid decrease in the magnitude of resistivity is seen at  $T < 10$  K for  $x > 0.6$ , indicating that the spin-flip scattering is reduced due to the FM ordering. The FM correlation of  $\text{Ce}^{3+}$  moments is also supported by the negative magnetoresistance shown in the inset of Fig. 2(b).

The evolution of electronic states can be further manifested by the specific heat measurement, displayed in Fig. 6(a). All the five measured samples,  $x = 0, 0.15, 0.53, 0.7$ , and  $1$ , show a

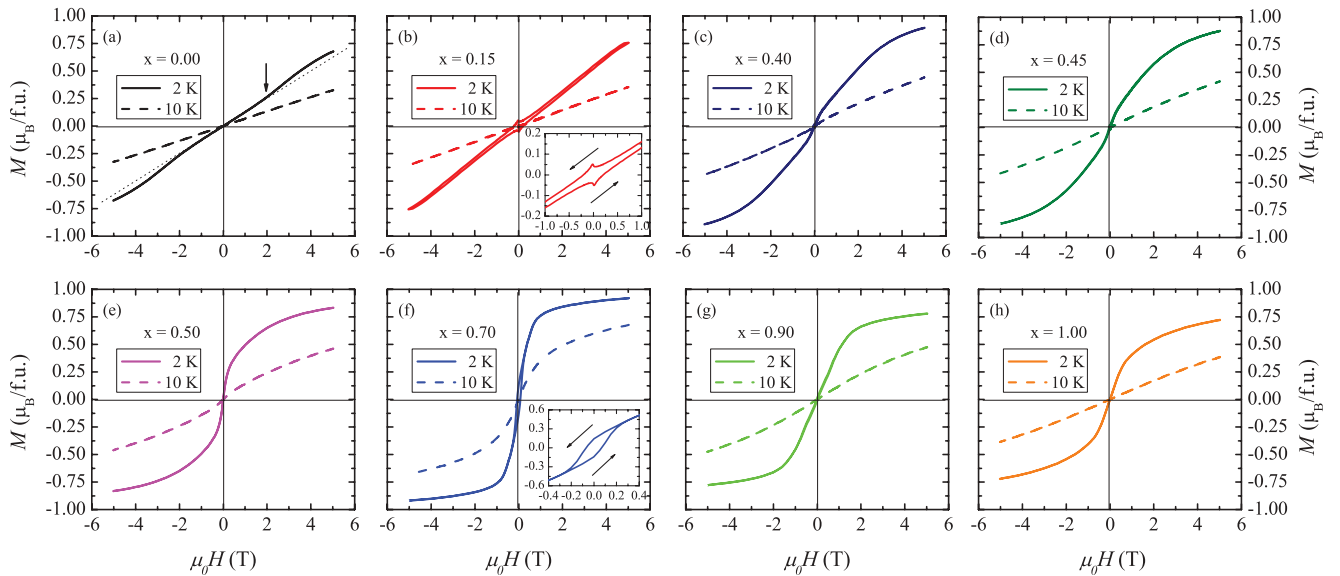


FIG. 5. (Color online) Isothermal magnetization of  $\text{CeFeAs}_{1-x}\text{P}_x\text{O}_{0.95}\text{F}_{0.05}$ . (a)  $x = 0$ , (b)  $x = 0.15$ , (c)  $x = 0.4$ , (d)  $x = 0.45$ , (e)  $x = 0.5$ , (f)  $x = 0.7$ , (g)  $x = 0.9$ , and (h)  $x = 1.0$ . For clarity, only the data for 2 K (solid lines) and 10 K (dashed lines) are shown. Arrow in (a) signifies the kink where  $M$  starts to deviate from the linear  $H$  dependence. The insets of (b) and (f) display the magnetic hysteresis loop at 2 K of  $x = 0.15$  and  $0.70$ .



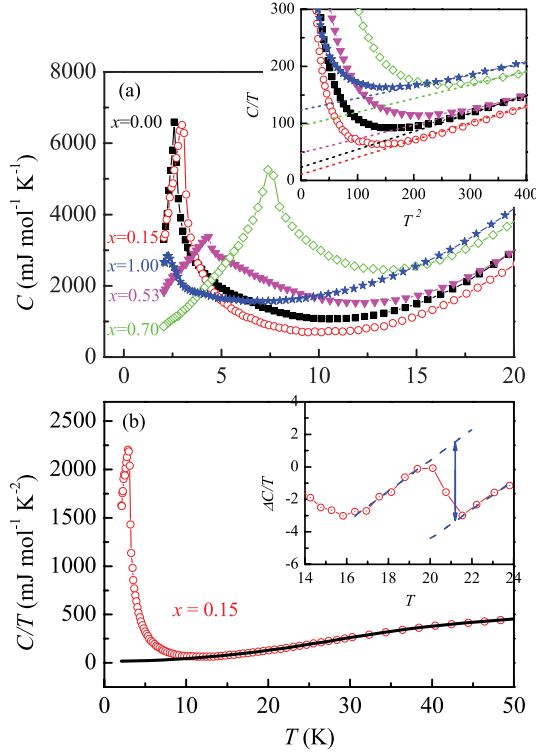


FIG. 6. (Color online) (a) Specific heat versus temperature of  $x = 0, 0.15, 0.53, 0.7$ , and  $1$  samples. Inset:  $C/T$  versus  $T^2$  plot to show the estimate of  $\gamma_0$ . (b) Specific heat jump of  $x = 0.15$  sample at the SC transition with the black line signifying the fit of Eq. (1).

$\lambda$ -shaped peak at low temperatures, indicating a second-order phase transition. These peaks are associated with either the AFM or the FM transition of the Ce 4*f* local moments. The residual Sommerfeld coefficient  $\gamma_0$ , estimated by extrapolating the  $C/T$  versus  $T^2$  curve to the zero limit, is plotted in the inset of Fig. 7. An increasing trend is clearly seen in  $\gamma_0$  as the sample is doped with P, although a minimum is observed around  $x = 0.15$ . Since  $\gamma_0$  is proportional to the density of states at the Fermi level, the small magnitude of  $\gamma_0$  in  $x = 0.15$  could be caused by the SC gap. The Sommerfeld coefficient for  $x = 1$  is about  $120.7 \text{ mJ/mol K}^2$ , which is about 15 times that of  $\text{LaFePO}_{0.95}\text{F}_{0.05}$  ( $8.3 \text{ mJ/mol K}^2$ ),<sup>22</sup> manifesting the correlated effect contributed from the Ce 4*f* electrons. Please note that the Schottky anomaly should not contribute much to the enhanced  $\gamma_0$ . Actually, the Schottky anomaly is expected to appear at a much higher temperature according to the studies of the CEF effect in CeFePO (Ref. 11) and CeFeAsO (Ref. 24), which should have a CEF effect similar to that in CeFeAs<sub>1-x</sub>P<sub>x</sub>O<sub>0.95</sub>F<sub>0.05</sub>. The good linearity in the plot of  $C/T$  versus  $T^2$  in a temperature range above the magnetic transition, as shown in the inset of Fig. 6(a), also implies that the Schottky anomaly should appear at a far higher temperature. Taking the crystal field energy levels for CeFeAsO<sub>0.84</sub>F<sub>0.16</sub> from Ref. 24, the calculation shows that the enhancement in  $\gamma_0$  due to the crystal field excitations should be less than 10% if only the specific heat data in the temperature range below 20 K are fitted. On the other hand, the presence of a magnetic peak in  $C(T)$  and the absence of  $\log(1/T)$  behavior in the  $C/T$ - $T$

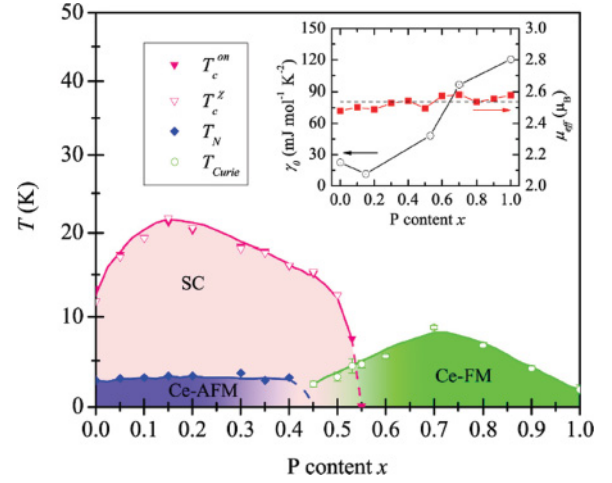


FIG. 7. (Color online) Electronic phase diagram of CeFeAs<sub>1-x</sub>P<sub>x</sub>O<sub>0.95</sub>F<sub>0.05</sub>. The pink region in the left side marks the superconductivity, with  $T_c^{\text{on}}$  and  $T_c^x$  representing transition temperatures defined from the  $\rho(T)$  and  $\chi(T)$  curves, respectively. The shaded regions in blue and green at the bottom signify antiferromagnetic and ferromagnetic orderings of Ce 4*f* moments, with  $T_N$  and  $T_{\text{Curie}}$  their characteristic temperatures. The inset shows the residual Sommerfeld coefficient  $\gamma_0$  as a function of P content  $x$ . The effective moment obtained from the Curie-Weiss fitting,  $\mu_{\text{eff}}$ , is also plotted in the inset, with the dashed line indicating  $2.54\mu_B$ , which is the effective moment of a free Ce<sup>3+</sup> ion.

curve [see Fig. 8(d)] suggest that it is an enhanced correlated ferromagnet, rather than a paramagnetic HF metal.

For the optimally doped CeFeAs<sub>0.85</sub>P<sub>0.15</sub>O<sub>0.95</sub>F<sub>0.05</sub>, the data for the specific heat are further analyzed in Fig. 6(b). No obvious jump in  $C(T)$  at  $T_c$  can be seen from the raw data (please see the main frame), as in the cases of other 1111 systems reported previously.<sup>25,26</sup> The  $\lambda$ -shaped peak positioned at 2.9 K is attributed to the Ce<sup>3+</sup> AFM transition. For the normal state, i.e.,  $T > 21.5 \text{ K}$ , the experimental data

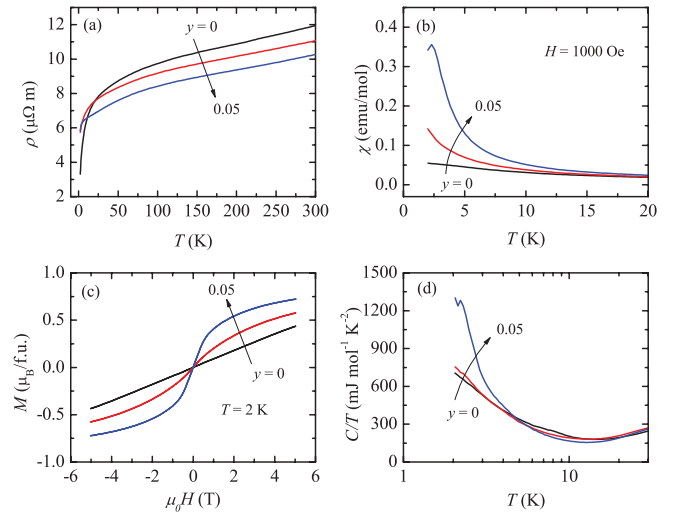


FIG. 8. (Color online) Physical properties of CeFePO<sub>1-y</sub>F<sub>y</sub>,  $y = 0$  (black),  $0.02$  (red), and  $0.05$  (blue): (a) temperature dependence of resistivity, (b) susceptibility, (c) isothermal field-dependent magnetization, and (d) specific heat.

can be well fitted by a combination of Debye's and Einstein's models,<sup>26,27</sup>

$$C(T) = \gamma T + A_D C_D(T, \theta_D) + A_E C_E(T, \theta_E), \quad (1)$$

where  $\gamma$  is the Sommerfeld coefficient, and  $C_D(T, \theta_D)$  and  $C_E(T, \theta_E)$  are Debye's function and Einstein's function, with  $\theta_D$  and  $\theta_E$  being their characteristic temperatures, respectively. The parameters derived from this analysis are  $\gamma = 15.3$  mJ/mol K<sup>2</sup>,  $\theta_D = 270.6$  K, and  $\theta_E = 351.4$  K. To investigate the SC properties, we subtract the fitted results from the raw data. An anomaly around  $T_c$  is clearly seen, with the jump  $\Delta C/T|_{T_c} \approx 5$  mJ/mol K<sup>2</sup>, much smaller than those of 122 and 111 systems.<sup>28,29</sup> This can be attributed to the gap modulation in the  $k_z$ -axis dispersion.<sup>30</sup> The jump in the specific heat around  $T_c$  is consistent with the large volume fraction of magnetic shielding derived from the susceptibility. The extrapolated residual specific heat coefficient  $\gamma_0$  is 11.5 mJ/mol K<sup>2</sup>. Note that this relatively large  $\gamma_0$  might be contributed by magnetic impurities and/or those bands in which Cooper pairs are not formed.

#### D. Phase diagram and discussion

An electronic phase diagram is proposed in Fig. 7 to summarize the experimental results. SC is observed in the P doping range  $0 \leq x < 0.55$ , with a maximal  $T_c^{\text{on}} \approx 21.3$  K around the optimal doping  $x = 0.15$ . Meanwhile, the ground state of Ce<sup>3+</sup> 4*f* local moments shows a long-range magnetic order, which changes from AFM to FM around  $x = 0.45$ . SC is found to coexist with Ce AFM at  $0 \leq x \lesssim 0.45$  and with Ce FM at  $0.45 \lesssim x \lesssim 0.53$ , respectively. The SC reentrances caused by the Ce magnetism (AFM or FM) are clearly seen on the two boundaries of the SC phase,  $x = 0$  and  $0.53$ . The FM region persists to the highest-P-doping end,  $x = 1$ .

Now we turn to the interplay between SC and Ce 4*f* magnetism. While Ce 4*f* AFM order coexists with SC in a wide region  $0 \leq x \lesssim 0.45$  where  $T_c$  reaches a maximum around  $x$  of 0.15, the Ce 4*f* FM ordering exhibits a strong destructive effect on SC. A slope change is clearly seen in the plot of  $T_c$ - $x$  around  $x = 0.45$ , as shown in Fig. 7, and  $T_c$  drops greatly when Ce 4*f* long-range FM order emerges. What is more interesting is that once  $T_{\text{Curie}} > T_c$ , SC vanishes almost instantly. Actually, such a reentrant behavior in resistivity due to the 4*f* magnetism has also been observed in the Co-doped EuFe<sub>2</sub>As<sub>2</sub> system,<sup>31,32</sup> where FM was found to coexist with SC in a narrow doping range. Furthermore, a similar first-order-like transition was also observed in EuFe<sub>1.9</sub>Co<sub>0.1</sub>As<sub>2</sub> under high pressure,<sup>33</sup> where no signature of SC can be detected once  $T_{\text{Curie}}$  is tuned to surpass  $T_c$ . Since Eu<sup>2+</sup> has a larger local moment, this detrimental effect of Eu<sup>2+</sup> magnetism on SC is more distinct. These observations evidently point to a competition between *d*-electron SC pairing and Ce 4*f* magnetism: SC survives only when  $T_c > T_{\text{Curie}}$  and it vanishes when the FM order is more robust.

It is also interesting to compare the two systems CeFeAs<sub>1-x</sub>P<sub>x</sub>O<sub>0.95</sub>F<sub>0.05</sub> and CeFeAs<sub>1-x</sub>P<sub>x</sub>O. While they both show the AFM-to-FM evolution of Ce 4*f* moments upon P doping, two main differences should be noted: (i) SC is quite robust in the 5% F-doping case but is absent in the case of only P doping; (ii) the HF behavior is evident in the case of only P doping but is absent in the 5% F doping case. We

remark that these interesting features reflect the different roles played by the F-O and P-As substitutions, which in turn tune the 3*d*-4*f* electron correlations in a delicate way: While P doping does not introduce extra electrons into the FeAs layer but increases the intrinsic itinerancy of the *d* electrons and significantly enhances the interlayer *d*-*f* coupling or Kondo effect, the effect of F doping is complicated and twofold. At the CeFeAsO end, F doping introduces extra electrons into the FeAs layer, thus suppressing the *d*-electron AFM via the band-filling effect, and moderately increases the interlayer *d*-*f* coupling, but at the CeFePO end, this interlayer coupling is weakened due to F doping. As a further support, we present experimental data for CeFePO<sub>1-y</sub>F<sub>y</sub> in the Appendix. We find that the Kondo effect is indeed reduced in the F-doped CeFePO compounds where the HF-FM crossover is evident. Owing to the relatively large specific heat coefficient seen in Fig. 8(d), these compounds represent a Kondo lattice system with coexistence of partial Kondo screening and FM ordering. This feature persists in CeFeAs<sub>1-x</sub>P<sub>x</sub>O<sub>0.95</sub>F<sub>0.05</sub>, as is evidenced by the enhanced  $\gamma_0$ , shown in the inset of Fig. 7, which reaches 50–120 mJ/mol K<sup>2</sup>, much larger than for the La-based counterparts. This strong enhancement mainly results from the 4*f* correlation effect.

Finally, we notice a salient feature of the F doping case: although the ionic radius of F<sup>-</sup> is smaller than that of O<sup>2-</sup>, the *c* axis of CeFeAs<sub>1-x</sub>P<sub>x</sub>O<sub>0.95</sub>F<sub>0.05</sub> is larger than that of CeFeAs<sub>1-x</sub>P<sub>x</sub>O when  $x > 0.45$  (see the inset of Fig. 1). This supports the previous expectation that the Kondo coupling is weaker in the F doping case. As is known, compared with FeAs-based compounds, FeP-based compounds exhibit more obvious three dimensionality,<sup>34</sup> and a two-dimensional (2D) hole cylinder present in the former case transforms into a pocket with three-dimensional (3D) dispersion in the latter. As F is doped, extra electrons are introduced, and the 3D pocket diminishes, leading to a more 2D property and a weakened interlayer *d*-*f* coupling. This is one possible interpretation of the slight increase of the *c* axis at the CeFePO end, and it could be responsible for the absence of HF behavior at that end.

#### IV. CONCLUSION

In summary, we have systematically studied the physical properties of CeFeAs<sub>1-x</sub>P<sub>x</sub>O<sub>0.95</sub>F<sub>0.05</sub> ( $0 \leq x \leq 1$ ) and a phase diagram is obtained. Both the *a* and *c* axes decrease monotonically with increasing P content, which effectively tunes the interlayer *d*-*f* coupling. SC is observed in the region  $0 \leq x < 0.55$  with a maximum  $T_c^{\text{on}}$  of 21.3 K. Reentrant behaviors are observed at the two SC boundaries of  $x = 0$  and  $0.53$ , due to Ce<sup>3+</sup> AFM and FM ordering, respectively. An AFM-to-FM evolution of Ce 4*f* electrons is observed near  $x \approx 0.45$ . No paramagnetic HF behavior is identified in the  $x = 1$  sample down to 2 K. Our studies indicate that SC can coexist with Ce 4*f* AFM order, but strongly competes with long-range Ce 4*f* FM order. SC can survive only when  $T_c > T_{\text{Curie}}$ . Combined with our previous studies on CeFeAs<sub>1-x</sub>P<sub>x</sub>O doped only with P,<sup>12</sup> the present results display the delicate band-filling and volume-contraction effects in F- and P-codoped CeFeAsO compounds, and provide clear evidence for the competition between the *d*-electron SC and the *d*-*f* coupling in rare-earth iron pnictides.

## ACKNOWLEDGEMENTS

This work is supported by the National Science Foundation of China (Grants No. 10634030 and No. 10931160425), the Fundamental Research Funds for the Central Universities of China (Program No. 2010QNA3026), and the National Basic Research Program of China (Grants No. 2011CBA00103 and No. 2010CB923003).

APPENDIX: CeFePO<sub>1-y</sub>F<sub>y</sub>

We have also studied the physical properties of single-phase CeFePO<sub>1-y</sub>F<sub>y</sub> ( $y = 0, 0.02$ , and  $0.05$ ). The synthesis process

is analogous to that of CeFeAs<sub>1-x</sub>P<sub>x</sub>O<sub>0.95</sub>F<sub>0.05</sub>. The main experimental data are shown in Fig. 8, in which some prominent features can be seen: (i) As F is doped, the crossover of coherent Kondo scattering in the  $\rho(T)$  curve disappears, replaced by a clear inflection at low temperatures, indicating a decrease of the spin-flip scattering. (ii) Both the susceptibility  $\chi(T)$  and field-dependent magnetization  $M(H)$  suggest the formation of the long-range FM order of the Ce 4*f* local moment upon F doping. (iii) A magnetic peak is observed in the specific heat in the sample with  $y = 0.05$ , and it is far away from  $\log(1/T)$  behavior. These results indicate that the HF behavior (which is observed in CeFePO) vanishes and the FM ordering of Ce 4*f* local moments emerges upon F doping in CeFePO.

\*zhuan@zju.edu.cn

- <sup>1</sup>Y. Kamihara, T. Watanabe, M. Hirano, and H. Hosono, *J. Am. Chem. Soc.* **130**, 3296 (2008).
- <sup>2</sup>X. H. Chen, T. Wu, G. Wu, R. H. Liu, H. Chen, and D. F. Fang, *Nature (London)* **453**, 761 (2008).
- <sup>3</sup>G. F. Chen, Z. Li, D. Wu, G. Li, W. Z. Hu, J. Dong, P. Zheng, J. L. Luo, and N. L. Wang, *Phys. Rev. Lett.* **100**, 247002 (2008).
- <sup>4</sup>H. H. Wen, G. Mu, L. Fang, H. Yang, and X. Zhu, *Europhys. Lett.* **82**, 17009 (2008).
- <sup>5</sup>H. Takahashi, K. Igawa, K. Arii, Y. Kamihara, M. Hirano, and H. Hosono, *Nature (London)* **453**, 376 (2008).
- <sup>6</sup>Z. Ren, G. Che, X. Dong, J. Yang, W. Lu, W. Yi, X. Shen, Z. Li, L. Sun, F. Zhou, and Z. Zhao, *Europhys. Lett.* **83**, 17002 (2008).
- <sup>7</sup>C. Wang, L. Li, S. Chi, Z. Zhu, Z. Ren, Y. Li, Y. Wang, X. Lin, Y. Luo, X. Xu, G. Cao, and Z. Xu, *Europhys. Lett.* **83**, 67006 (2008).
- <sup>8</sup>R. Pottgen and D. Johrendt, *Z. Naturforsch. B: Chem. Sci.* **63**, 1135 (2008).
- <sup>9</sup>C. de la Cruz, Q. Huang, J. W. Lynn, J. Li, W. Ratcliff II, J. L. Zarestky, H. A. Mook, G. F. Chen, J. L. Luo, N. L. Wang, and P. Dai, *Nature (London)* **453**, 899 (2008).
- <sup>10</sup>J. Zhao, Q. Huang, C. de la Cruz, S. Li, J. W. Lynn, Y. Chen, M. A. Green, G. F. Chen, G. Li, Z. Li, J. L. Luo, N. L. Wang, and P. Dai, *Nature Mater.* **7**, 953 (2008).
- <sup>11</sup>E. M. Brüning, C. Krellner, M. Baenitz, A. Jesche, F. Steglich, and C. Geibel, *Phys. Rev. Lett.* **101**, 117206 (2008).
- <sup>12</sup>Y. Luo, Y. Li, S. Jiang, J. Dai, G. Cao, and Z. A. Xu, *Phys. Rev. B* **81**, 134422 (2010).
- <sup>13</sup>J. Dai, Q. Si, J. X. Zhu, and E. Abrahams, *Proc. Natl. Acad. Sci. USA* **106**, 4118 (2009).
- <sup>14</sup>J. Dai, J. X. Zhu, and Q. Si, *Phys. Rev. B* **80**, 020505(R) (2009).
- <sup>15</sup>C. Wang, S. Jiang, Q. Tao, Z. Ren, Y. Li, L. Li, C. Feng, J. Dai, G. Cao, and Z. Xu, *Europhys. Lett.* **86**, 47002 (2009).
- <sup>16</sup>S. Jiang, H. Xing, G. Xuan, C. Wang, Z. Ren, C. Feng, J. Dai, Z. Xu, and G. Cao, *J. Phys. Condens. Matter* **21**, 382203 (2009).
- <sup>17</sup>S. Kasahara, T. Shibauchi, K. Hashimoto, K. Ikada, S. Tonegawa, R. Okazaki, H. Shishido, H. Ikeda, H. Takeya, K. Hirata, T. Terashima, and Y. Matsuda, *Phys. Rev. B* **81**, 184519 (2010).
- <sup>18</sup>Z. Ren, Q. Tao, S. Jiang, C. Feng, C. Wang, J. Dai, G. Cao, and Z. Xu, *Phys. Rev. Lett.* **102**, 137002 (2009).
- <sup>19</sup>C. de la Cruz, W. Z. Hu, S. Li, Q. Huang, J. W. Lynn, M. A. Green, G. F. Chen, N. L. Wang, H. A. Mook, Q. Si, and P. Dai, *Phys. Rev. Lett.* **104**, 017204 (2010).
- <sup>20</sup>H. Luetkens, H.-H. Klauss, M. Kraken, F. J. Litterst, T. Dellmann, R. Klingeler, C. Hess, R. Khasanov, A. Amato, C. Baines, M. Kosmala, O. J. Schumann, M. Braden, J. Hamann-Borrero, N. Leps, A. Kondrat, G. Behr, J. Werner, and B. Büchner, *Nature Mater.* **8**, 305 (2009).
- <sup>21</sup>A. J. Drew, Ch. Niedermayer, P. J. Baker, F. L. Pratt, S. J. Blundell, T. Lancaster, R. H. Liu, G. Wu, X. H. Chen, I. Watanabe, V. K. Malik, A. Dubroka, M. Rössle, K. W. Kim, C. Baines, and C. Bernhard, *Nature Mater.* **8**, 310 (2009).
- <sup>22</sup>S. Suzuki, S. Miyasaka, S. Tajima, T. Kida, and M. Hagiwara, *J. Phys. Soc. Jpn.* **78**, 114712 (2009).
- <sup>23</sup>A. Jesche, C. Krellner, M. de Souza, M. Lang, and C. Geibel, *New J. Phys.* **11**, 103050 (2009).
- <sup>24</sup>S. Chi, D. T. Adroja, T. Guidi, R. Bewley, S. Li, J. Zhao, J. W. Lynn, C. M. Brown, Y. Qiu, G. F. Chen, J. L. Lou, N. L. Wang, and P. Dai, *Phys. Rev. Lett.* **101**, 217002 (2008).
- <sup>25</sup>G. Mu, X. Y. Zhu, L. Fang, L. Shan, C. Ren, and H. H. Wen, *Chin. Phys. Lett.* **25**, 2221 (2008).
- <sup>26</sup>P. J. Baker, S. R. Giblin, F. L. Pratt, R. H. Liu, G. Wu, X. H. Chen, M. J. Pitcher, D. R. Parker, S. J. Clarke, and S. J. Blundell, *New J. Phys.* **11**, 025010 (2009).
- <sup>27</sup>M. Tropeano, A. Martinelli, A. Palenzona, E. Bellingeri, E. Galleani d'Agliano, T. D. Nguyen, M. Affronte, and M. Putti, *Phys. Rev. B* **78**, 094518 (2008).
- <sup>28</sup>G. Mu, H. Luo, Z. Wang, L. Shan, C. Ren, and H. H. Wen, *Phys. Rev. B* **79**, 174501 (2009).
- <sup>29</sup>F. Wei, F. Chen, K. Sasmal, B. Lv, Z. J. Tang, Y. Y. Xue, A. M. Guloy, and C. W. Chu, *Phys. Rev. B* **81**, 134527 (2010).
- <sup>30</sup>J. P. Reid, M. A. Tanatar, X. G. Luo, H. Shakeripour, N. D. Leyraud, N. Ni, S. L. Bud'ko, P. C. Canfield, R. Prozorov, and L. Taillefer, *Phys. Rev. B* **82**, 064501 (2010).
- <sup>31</sup>S. Jiang, H. Xing, G. Xuan, Z. Ren, C. Wang, Z. A. Xu, and G. Cao, *Phys. Rev. B* **80**, 184514 (2009).
- <sup>32</sup>Y. He, T. Wu, G. Wu, Q. J. Zheng, Y. Z. Liu, H. Chen, J. J. Ying, R. H. Liu, X. F. Wang, Y. L. Xie, Y. J. Yan, J. K. Dong, S. Y. Li, and X. H. Chen, *J. Phys. Condens. Matter* **22**, 235701 (2010).
- <sup>33</sup>M. Nicklas, M. Kumar, E. Lengyel, W. Schnelle, and A. Leithe-Jasper, e-print [arXiv:1006.3471](https://arxiv.org/abs/1006.3471).
- <sup>34</sup>V. Vildosola, L. Pourvorskii, R. Arita, S. Biermann, and A. Georges, *Phys. Rev. B* **78**, 064518 (2008).